

High-performance Sn–Ni alloy nanorod electrodes prepared by electrodeposition for lithium ion rechargeable batteries

Dongdong Jiang · Xiaohua Ma · Yanbao Fu

Received: 31 December 2011 / Accepted: 13 May 2012 / Published online: 3 June 2012
© Springer Science+Business Media B.V. 2012

Abstract To reduce irreversible capacity and improve cycle performance of tin used in lithium ion batteries, Sn–Ni alloy nanorod electrodes with different Sn/Ni ratios were prepared by an anodic aluminum oxide template-assisted electrodeposition method. The structural and electrochemical performance of the electrode were characterized using scanning electron microscopy, energy dispersive X-ray spectroscopy, X-ray diffraction, cyclic voltammetry, and galvanostatic charge–discharge cycling measurement. The results showed that the copper substrate is covered with uniformly distributed Sn–Ni alloy nanorods with an average diameter of 250 nm. Different phases (Sn, Ni_3Sn_4 and metastable phases) of alloy nanorod formed in the electrodeposition baths with different compositions of Sn^{2+} and Ni^{2+} ions. Sn–Ni alloy nanorod electrode delivered excellent capacity retention and rate performance.

Keywords Sn–Ni alloy · Nanorods · Electrodeposition · Lithium ion batteries

1 Introduction

Rechargeable lithium ion batteries with high-energy capacity and long cycle life are being widely used in portable electronic devices, electric vehicles and implantable medical devices [1–7]. Tin is a promising anode material for lithium ion batteries because of its low charge potential and large theoretical capacity (991 mAh g^{-1}) [8]. Although it is equivalent to about 2.5 times of the capacity of graphite, tin anode has limited application because of its large volume change up to

360 % in the process of alloying and dealloying of Li–Sn, which leads to pulverization and capacity fading [7–13].

In order to improve the cycle performance of electrode, researchers have tried to modify the electrode structure [14]. Extensive attention has been paid on tin-based intermetallic compounds, such as Sn–Co [15–17], Sn–Sb [18], Sn–Ni [19], etc. These materials exhibit longer cyclability than pure tin. The inactive element can buffer the large volume change as a barrier against the aggregation of tin into large grains during alloying and dealloying process of Li–Sn [11, 18]. However, large capacity loss still happened after long-term cycling.

One-dimensional nanorod materials, such as nanorods of Si [1], SnO_2 [7, 20], Co_3O_4 [21], and TiO_2 [22], have shown some improvement in the rate capability and cycle performance compared with film and bulk materials. The nanorod structure has several advantages [1–3, 14, 23]. First, nanorod with one-dimensional nanostructure allows for better accommodation of the large volume change of metallic anode materials. Second, the nanorod electrode allows for fast surface reaction originating from large electrode/electrolyte interface area. Third, the nanorod electrode has a short Li-ion transport length compared to bulk materials.

In this article, a new Sn–Ni alloy nanorod electrode, which is expected to accommodate large strain and reduce the Li-ion diffusion length, has been prepared by an anodic aluminum oxide (AAO) template-assisted electrodeposition method.

2 Experimental

2.1 Fabrication of Sn–Ni alloy nanorod electrodes

Sn–Ni alloy nanorods on copper sheet substrate were fabricated by cathodic electrodeposition in an electrodeposition

D. Jiang · X. Ma · Y. Fu (✉)
Department of Materials Science, Fudan University, Shanghai
200433, China
e-mail: yanbaofu@fudan.edu.cn

bath described in Table 1, inside the pores of the AAO membrane (Whatman, Anodisc 13, Cat. no. 6809–7013). The AAO membrane is with a thickness of 60 μm , a diameter of 13 mm, and a pore size of 200 nm. The AAO membrane was sandwiched between a metallic copper sheet and a platinum sheet. The copper sheet served as the cathode, and the Pt sheet served as the anode. The copper surface was thoroughly polished to ensure good contact with the membrane. The electrodeposition was carried out at a constant current of 10 mA cm^{-2} . After the electrodeposition, the cathodes were immersed in a 5.0 mol L^{-1} sodium hydroxide solution to remove the AAO templates and then cleaned in an acidic sulfate solution to remove the surface oxides. The as-prepared samples were stored in a glove box preventing them from further oxidation. For comparison, the planar tin anodes were also prepared by directly electrodepositing tin onto a copper foil in the same condition as that of nanorod electrode.

2.2 Structure and morphology characterization

The as-prepared Sn–Ni alloy nanorod electrodes were characterized by X-ray diffraction (XRD, RIGAKU D/MAX- γ B, CuK_α) and field emission scanning electron microscopy (FE-SEM, Philips XL30) equipped with energy-dispersive X-ray (EDX) spectroscopy.

2.3 Electrochemical performance tests

The electrochemical performance of Sn–Ni alloy nanorod electrodes was evaluated using coin-type cells. Coin-type cells were assembled with Sn nanorods on the copper substrate as the positive electrode and lithium metals as the negative electrode. Both the positive and negative electrodes were electronically separated by Celgard 2400 separator saturated with 1 mol L^{-1} LiPF_6 electrolyte solution (in EC:EMC:DMC/1:1:1 in mass ratio). Cyclic voltammetry (CV) measurement was carried out in the potential range of

0–2.0 V (vs. Li/Li^+), at a scan rate of 0.1 mV s^{-1} . The charge/discharge capacities and the capacity retention property of Sn–Ni nanorods electrodes at different charge/discharge current rates were measured by galvanostatic charge and discharge tests (the discharge capacity in this research is the total charge inserted into the Sn nanorod, per mass unit, during alloying process of Li–Sn, while the charge capacity is the total charge during dealloying process of Li–Sn).

3 Results and discussion

3.1 Morphologic and structural characterization of Sn–Ni alloy nanorods

The composition of Sn–Ni alloy nanorods prepared in different electrodeposition baths was determined by EDX shown in Fig. 1. From EDX spectra, tin, and nickel peaks were detected. The tin atom percent of Sn–Ni alloy nanorods is 54 % (NR54), 70 % (NR70), 78 % (NR78), and 100 % (NR100), corresponding to B-1, B-2, B-3, and B-4, respectively.

The XRD patterns of Sn–Ni alloy prepared with different tin atom percent are presented in Fig. 2. The strongest peaks around 43.3° and 50.3° correspond to the Cu (111) and Cu (200) reflections, respectively, originating from the copper substrate. For sample NR54, in addition to Cu (111) and Cu (200), we can observe one peak at around 30.4° corresponding to Ni_3Sn_4 (111) (JCPDS card no. 4-0851) and no obvious peaks corresponding to pure tin appeared. For sample NR70, several peaks observed at 30.6°, 32.0°, and

Table 1 The formulation of electrodeposition bath for preparing Sn–Ni alloy electrodes

Formulation	Bath no.			
	B-1	B-2	B-3	B-4
$\text{NiCl}_2 \cdot 6\text{H}_2\text{O}$ (mol L^{-1})	0.125	0.075	0.063	0
$\text{SnCl}_2 \cdot 2\text{H}_2\text{O}$ (mol L^{-1})	0.125	0.175	0.187	0
$\text{K}_4\text{P}_2\text{O}_7$ (mol L^{-1})	0.500	0.500	0.500	0
$\text{H}_2\text{NCH}_2\text{COOH}$ (mol L^{-1})	0.250	0.125	0.100	0
NH_4OH (mol L^{-1})	5	5	5	0
SnSO_4 (mol L^{-1})	0	0	0	0.116
H_2SO_4 (mol L^{-1})	0	0	0	0.408
Gelatin (g L^{-1})	0	0	0	20

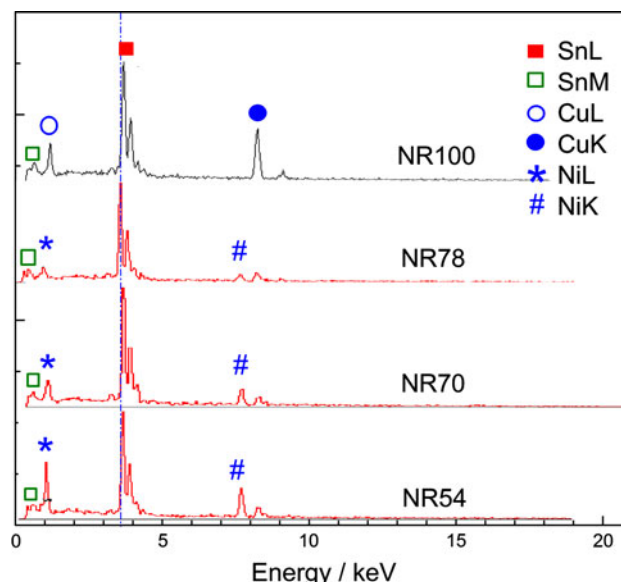


Fig. 1 EDX spectra of Sn–Ni alloy nanorods on the copper current collector

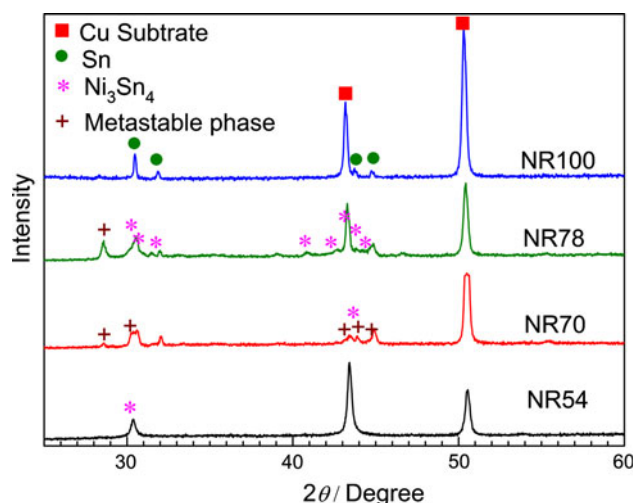


Fig. 2 XRD patterns of Sn–Ni alloy nanorods on the copper current collector

44.9° are assigned to (200), (101), and (211) reflections of tin (JCPDS card no. 89-2958). The peak at 43.8° is assigned to (312) reflection of Ni_3Sn_4 (JCPDS card no. 4-0851). Some weak peaks appeared around 28.5°, 30.4°, 43.0°, and 45.0°, which can be assigned to metastable phases of Sn–Ni alloy defined by Watanabe et al. [24] who carried out detailed research on structure of electrodeposited Sn–Ni alloy film. In their research, metaphases are defined as the phases that do not appear in the equilibrium phase diagram, such as Ni–Sn and other phases, where Ni diffused into pure Sn crystal lattice which formed because of the electrodeposition process. For sample NR78, the XRD pattern indicates the presence of two main phase: Ni_3Sn_4 and Sn, evidenced by the main peaks at 30.3°, 31.5°, 43.8°, and 44.6° assigned to (111), (310), (312), (020) reflection of Ni_3Sn_4 (JCPDS card no. 4-0851) and peaks at 30.6°, 32.0°, and 44.9° assigned to (200), (101), and (211) reflections of Sn. Compared to NR70, most diffraction peaks assigned to metastable phases disappeared. For sample NR100, in addition to Cu (111) and Cu (200) peaks from copper substrate, diffraction peaks assigned to Sn (200), (101), and (211) reflections of Sn nanorods were observed. In addition, for NR54 the peak intensity of Cu (111) is higher than that of Cu (200) and for other samples, it is the opposite. It may be caused by the textural effect of the substrate. The results of XRD pattern indicated that the different phases of alloy nanorod formed in the electrodeposition baths with different compositions of Sn^{2+} and Ni^{2+} ions.

Figure 3 shows typical top and cross views of Sn–Ni alloy (NR70) nanorods by FE-SEM. From SEM images it is observed that copper substrate is covered with uniformly distributed Sn–Ni alloy nanorods, with an average diameter of 250 nm. The nanorods have larger diameters than the nominal pore diameter of the AAO template. It is possible

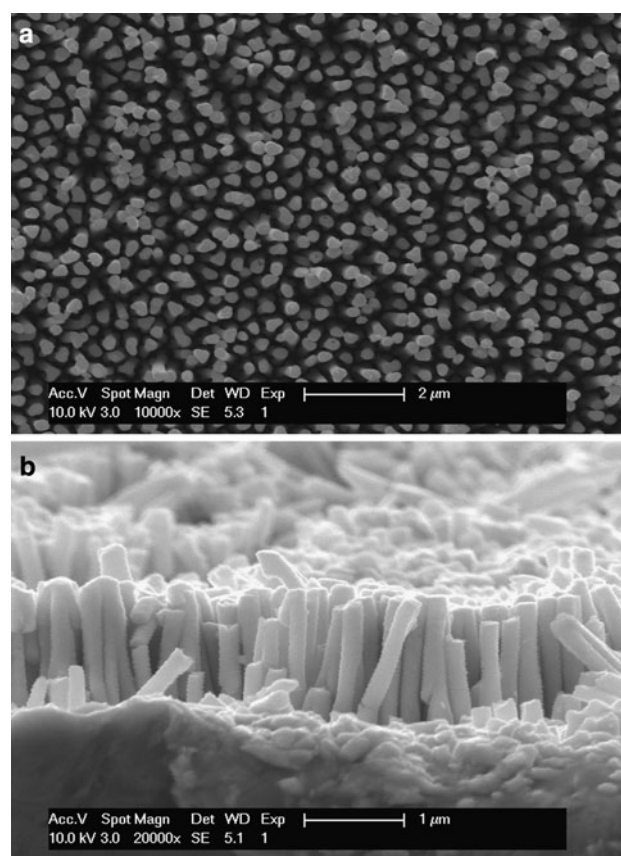


Fig. 3 SEM images of Sn–Ni alloy nanorods (NR70). **a** top view. **b** cross-sectional view

that the nanorods expanded with strain release, after the AAO template was removed. The inter-rod distance was measured to be about several hundred nanometers, which is crucial to gain the advantage of nanostructure such as large surface area, reducing Li-ion diffusion path and buffering space.

The electrochemical properties of the Sn–Ni nanorod electrodes were evaluated by cyclic voltammetry and galvanostatic cycling using coin-type half cell. For comparison, the electrochemical performance of counterpart planar electrodes was also measured.

Cyclic voltammogram of Sn–Ni alloy (NR70) nanorod electrode (with 0.1 mV s^{-1} scan rate) is shown in Fig. 4. Three cathodic current peaks at 0.65, 0.33, and 0 V; and four anodic current peaks at 0.52, 0.64, 0.74, and 0.81 V were assigned to the alloying and dealloying of lithium with tin, respectively [11]. For instance, the peak at 0.65 V corresponds to the formation of Li–Sn phase, and the peak at 0.33 V is associated with the formation of $\text{Li}_{22}\text{Sn}_5$ phase. It was observed that there is a little difference between the first cycle and the following cycles, and fewer peaks in the first cycle. This may be caused by the electrode polarization and the formation of solid electrolyte interface (SEI) film. The magnitude of the current peaks increased with

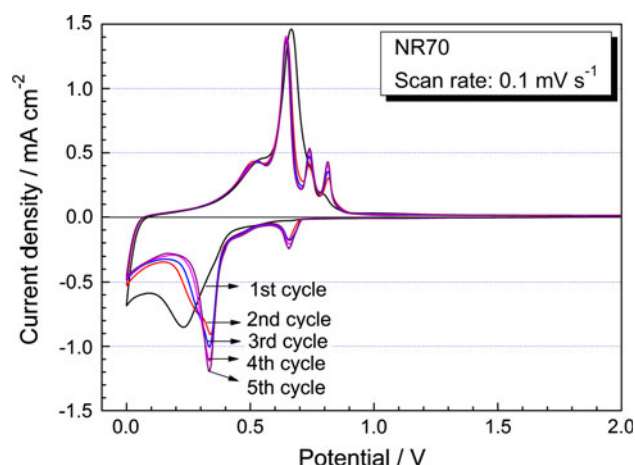


Fig. 4 Cyclic voltammogram for NR70 electrode from 2.0–0 V with 0.1 mV s⁻¹ scan rate

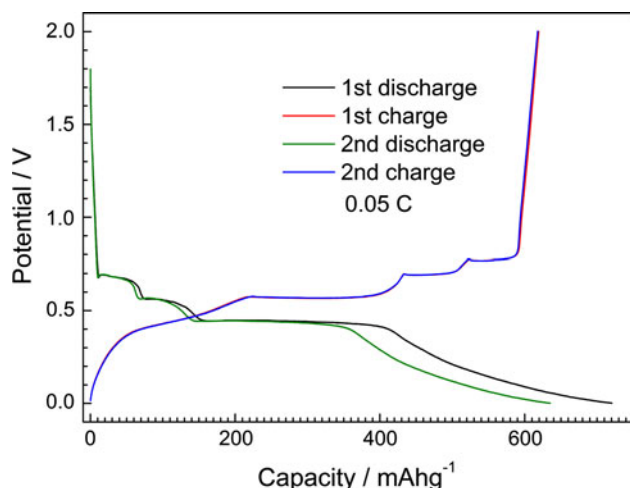


Fig. 5 Voltage profiles for the 1st and the 2nd galvanostatic cycles of Sn–Ni nanorod electrode (NR70) at 0.05-C current rate

cycling due to activation of more material to react with Li in each scan.

Figure 5 shows the typical voltage profile of Sn–Ni nanorod electrode (NR70) for 1st and 2nd cycles with 0.05-C current rate. The voltage profiles show several long plateaus below 0.70 V during the discharge process, associated with the formation of the Li_xSn alloy; and several long plateaus during the charge process, corresponding to dealloying of Li_xSn , which is consistent with the cyclic voltammetric result.

Figure 6 compares the cycling behaviors at the 0.1-C rate (10 h per half cycle) for prepared nanorod electrodes. For samples with same composition of Sn and Ni, the nanorod electrode shows better cyclic performance than that of planar one. For NR54, although in the 2nd cycle the charge capacity decreased from initial capacity of 400.1–296.7 mAh g⁻¹, from the 3rd cycle, the charge

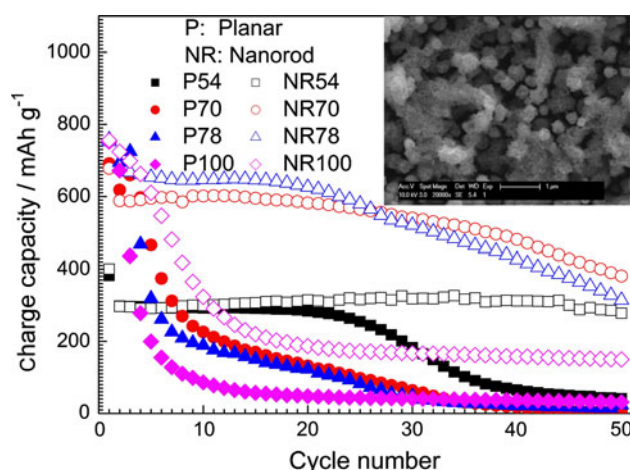


Fig. 6 Charge capacity versus cycle number for Sn–Ni alloy nanorod and planar electrodes at 0.1-C current rate. (The inserted SEM image corresponding to NR70 being charged and discharged 50 cycles.)

capacity grows gradually and it reached 326 mAh g⁻¹ at 35th cycle. From then, it remains almost constant. The Sn–Ni alloy nanorod electrode with Sn atom percent of 54 % shows excellent cycle performance. It should be attributed to the buffering effect of Ni phase during Li–Sn alloying and dealloying, since Ni is inactive in this process. Because the Ni phase is composed of the nanorod electrode, which was considered as electrochemically active material when the specific capacity was calculated, it leads to the low specific capacity compared with theoretical capacity of tin. Hence, for NR54 with high content of Ni, the excellent cycle performance is gained at the expense of reducing capacity. For NR70 and NR78, the initial reversible capacities reached 678.0 and 780.1 mAh g⁻¹, respectively. In the first 20 cycles, the samples showed good capacity retention performance, and the capacities are 582.0 and 625.7 mAh g⁻¹. However, in the following cycle, the capacity decreased slowly, and it faded to 381.0 mAh g⁻¹ at the 50th cycle for NR70. The capacity fading could be attributed to the partly pulverization of Sn during charge and discharge processes, just shown as inserted SEM image in Fig. 6. For pure tin nanorod electrode, in the initial 15 cycles, the capacity dropped rapidly from 757.8 mAh g⁻¹ at the 1st cycle to 186.8 mAh g⁻¹ at the 15th cycle, and then the capacity became stable.

As a comparison, our charge data are shown along with the charge capacities of corresponding thin film planar Sn–Ni alloy electrodes, which were fabricated by directly electrodepositing Sn–Ni alloy onto a copper foil. Although the initial charge capacity of thin film planar Sn–Ni alloy electrodes is higher than that of corresponding nanorod electrolyte, it faded rapidly in the following several cycles and after ten cycles, most of them faded to less than 200 mAh g⁻¹. The improved cycle life in the Sn–Ni alloy

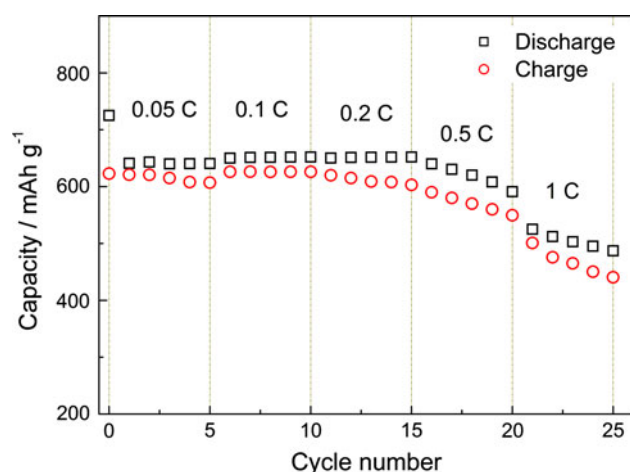


Fig. 7 Capacity versus cycle number for the Sn–Ni alloy nanorod electrode (NR70) at different current rates in the range of 0.05–1 C

nanorods should be related with the one-dimensional nanorod structure and the addition of the inactive nickel that can be served as a barrier against the aggregation of Sn into large grains during the Li-ion insertion and extraction process.

The rate performance of Sn–Ni alloy nanorods electrodes (NR70) was also evaluated. The Sn–Ni alloy nanorods also displayed excellent rate capability at high current rates. Figure 7 shows the discharge and charge capacities of the Sn–Ni alloy nanorod electrode at different current rates, in the range of 0.05–1 C. Even at the 1-C rate, the charge capacity is larger than 500 mAh g⁻¹. The capacity at the 0.1-C rate is larger than the capacity at the 0.05-C rate for the Sn–Ni alloy nanorod electrode, which is probably due to the activation of more material to react with lithium in the initial several cycles.

4 Conclusion

Sn–Ni alloy nanorod electrodes were prepared for Li-ion rechargeable batteries by an AAO template-assisted growth method. The copper current collector was covered with uniformly distributed Sn–Ni alloy nanorods, with an average diameter of about 250 nm. The Sn–Ni alloy nanorod electrode exhibited superior capacity retention and rate capability in comparison with pure tin nanorods and Sn–Ni alloy planar electrode. The nanorod electrodes structure and

formation of alloy phase can partly accommodate large volume expansion that leads to pulverization during cycling.

References

1. Chan CK, Peng HL, Liu G, McIlwrath K, Zhang XF, Huggins RA, Cui Y (2008) *Nat Nanotechnol* 3:31–35
2. Taberna PL, Mitra S, Poizot P, Simon P, Tarascon JM (2006) *Nat Mater* 5:567–573
3. Duan HN, Gnanaraj J, Chen XP, Li BQ, Liang JY (2008) *J Power Sources* 185:512–518
4. Bazin L, Mitra S, Taberna PL, Poizot P, Gressier M, Menu MJ, Barnabe A, Simon P, Tarascon JM (2009) *J Power Sources* 188:578–582
5. Idota Y, Kubota T, Matsufuji A, Maekawa Y, Miyasaka T (1997) *Science* 276:1395–1397
6. Poizot P, Laruelle S, Grugeon S, Dupont L, Tarascon JM (2000) *Nature* 407:496–499
7. Li NC, Martin CR, Scrosati B (2001) *J Power Sources* 97–98:240–243
8. Courtney IA, Dahn JR (1997) *J Electrochem Soc* 144:2045–2052
9. Whitehead AH, Elliott JM, Owen JR (1999) *J Power Sources* 81–82:33–38
10. Tamura N, Ohshita R, Fujimoto M, Kamino M, Fujitani SJ (2003) *J Electrochem Soc* 150:A679–A683
11. Winter M, Besenhard JO (1999) *Electrochim Acta* 45:31–50
12. Yang J, Wachtler M, Winter M, Besenhard JO (1999) *Electrochim Solid State Lett* 2:161–163
13. Lee SJ, Lee HY, Jeong SH, Baik HK, Lee SM (2002) *J Power Sources* 111:345–349
14. Ke FS, Huang L, Jiang HH, Wei HB, Yang FZ, Sun SG (2007) *Electrochem Commun* 9:228–232
15. Tamura N, Fujimoto M, Kamino M, Fujitani S (2004) *Electrochim Acta* 49:1949–1956
16. Fan X, Ke F, Wei G, Huang L, Sun S (2009) *J Alloy Compd* 476:70–73
17. He J, Zhao H, Wang J, Chen J (2010) *J Alloy Compd* 508:629–635
18. Wachtler M, Winter M, Besenhard JO (2002) *J Power Sources* 105:151–160
19. Chen X, Shi P (2005) *J Alloy Compd* 391:241–244
20. Park MS, Wang GX, Kang YM, Wexler D, Dou SX, Liu HK (2007) *Angew Chem Int Ed* 46:750–753
21. Shaju KM, Jiao F, Debart A, Bruce PG (2007) *Phys Chem Chem Phys* 9:1837–1842
22. Armstrong G, Armstrong AR, Bruce PG, Reale P, Scrosati B (2006) *Adv Mater* 18:2597–2600
23. Long JW, Dunn B, Rolison DR, White HS (2004) *Chem Rev* 104:4463–4492
24. Watanabe T, Hirose T, Arai K, Chikazawa M (1999) *J Jpn Inst Met* 63:496–501